











Direct temporal characterization of sub-3-fs deep UV pulses generated by resonant dispersive wave emission

M. REDUZZI,^{1,†} M. PINI,^{1,2,†}  L. MAI,¹ F. CAPPENBERG,¹ L. COLAIZZI,¹ F. VISMARRA,^{1,2}  A. CREGO,^{2,3}  M. LUCCHINI,^{1,2}  C. BRAHMS,⁴  J. C. TRAVERS,⁴  R. BORREGO-VARILLAS,²  AND M. NISOLI^{1,2,*} 

¹Department of Physics, Politecnico di Milano, Piazza Leonardo da Vinci 32, Milano 20133, Italy

²Institute for Photonics and Nanotechnologies-CNR (IFN-CNR), Piazza Leonardo da Vinci 32, Milano 20133, Italy

³Grupo de Investigación en Aplicaciones del Láser y Fotónica, Departamento de Física Aplicada, Universidad de Salamanca, E-37008 Salamanca, Spain

⁴School of Engineering and Physical Sciences, Heriot-Watt University, Edinburgh EH14 4AS, UK

[†]These authors contributed equally to this work

*mauro.nisoli@polimi.it

Abstract: We report on the complete temporal characterization of ultrashort pulses, generated by resonant dispersive wave emission in gas-filled hollow-capillary fibers, with energy in the microjoule range and continuously tunable from the deep-ultraviolet to the ultraviolet. Temporal characterization of such ultrabroad pulses, particularly challenging in this spectral region, was performed using an all-in-vacuum setup for self-diffraction frequency resolved optical gating (SD-FROG). Sub-3-fs pulses were measured, tunable from 250 nm to 350 nm, with a minimum pulse duration of 2.4 ± 0.1 fs.

© 2023 Optica Publishing Group under the terms of the [Optica Open Access Publishing Agreement](#)

1. Introduction

The generation of ultrashort light pulses, tunable in the deep ultraviolet (DUV) and in the ultraviolet (UV) spectral regions, is of crucial importance for a variety of experiments [1]. A particularly important class of applications is the investigation of ultrafast electronic and nuclear photo-induced processes in molecules with biological or optoelectronic relevance. Remarkable examples are nucleobases, aromatic amino acids, as well as donor-acceptor systems, which typically exhibit strong absorption bands centered in these spectral regions [2–6]. Moreover, short DUV/UV light pulses, with just few-cycle duration, which corresponds to sub-3-fs full-width half-maximum (FWHM) (3 cycles at 300 nm), are essential for the investigation of purely electronic processes in neutral molecules, possibly in combination with attosecond pulses in the extreme ultraviolet (EUV) or soft x-ray energy range [7–10]. This is currently a hot research topic since it would pose the basis for effective control of the ultrafast motion of electrons inside molecules. This motion could, in turn, influence the subsequent nuclear dynamics unfolding on a longer time scale [11,12]. While in the visible spectral region the generation of light pulses approaching the single-cycle regime is currently available, employing, for example, the hollow-capillary fiber (HCF) compression technique [13] or optical parametric processes in nonlinear crystals [14], in combination with ultra-broadband dispersion compensation, the extension of these methods to the DUV/UV region is extremely challenging [15]. In 2004 sub-10-fs pulses, tunable from 275 nm to 335 nm have been generated by achromatic frequency doubling of a nonlinear optical parametric amplifier [16]. The pulses have been characterized by zero-additional-phase spectral phase interferometry for direct electric field reconstruction (ZAP-SPIDER) [17]. Intense 8-fs

pulses at 270 nm have been generated by four-wave mixing (FWM) in HCFs [18]. By using chirped-pulse FWM in HCFs Kida *et al.* reported on the generation of negatively chirped DUV pulses, subsequently compressed to 9.7 fs by propagation in air [19]. In this case FWM was obtained by coupling in a gas-filled HCF a negatively chirped UV pulse and a positively chirped near infrared pulse. Third harmonic generation in gases was employed for the generation of sub-3-fs pulses at 260 nm [20]. So far, the shortest DUV pulses, with a duration of 1.9 fs at 260 nm central wavelength, were produced by third harmonic generation (THG) driven by few-fs near-infrared pulses in a high-pressure gas cell [21]. The main disadvantages of this technique are the small conversion efficiency, of the order of 7×10^{-4} , and the negligible spectral tunability.

In 2019, Travers and coworkers introduced a new experimental scheme for efficient generation of ultrashort pulses, tunable in an ultrabroad spectral range, based on the use of Resonant Dispersive Wave (RDW) emission in gas-filled HCFs [22]. Ultrashort and tunable pulses were reported, with energy in the microjoule range, thus increasing by up to three orders of magnitude the energy of the pulses, compared to that obtained by RDW emission in gas-filled anti-resonant photonic crystal fibers [23]. In brief, RDW emission, also known as non-solitonic or Čerenkov radiation, is a process occurring when a portion of the energy in a self-compressing soliton, which is propagating in a fiber, is transferred to a secondary pulse at a phase-matched shifted frequency, in the presence of higher-order dispersive effects [24–27]. The precise wavelength of the RDW component is determined by a phase-matching condition between the emitted radiation and the soliton pulse [28], and the dispersion profile in gas-filled HCF places the phase-matched point at a higher frequency.

Various techniques have been employed for the measurement of the duration of the RDW pulses. Nanojoule-scale DUV pulses generated by RDW emission in a gas-filled hollow-core photonic crystal fiber have been temporally characterized by transient-grating cross-correlation frequency-resolved optical gating (TG-XFROG): the estimated pulse duration was ~ 4 fs at 275 nm central wavelength [29]. In 2019, 30-nJ RDW pulses, tunable between 225 nm and 300 nm, generated in an anti-resonant photonic crystal fiber with pressure gradient have been measured by using in-vacuum XFROG [30]. Difference-frequency generation in a beta barium borate (BBO) crystal between the DUV pulse and an infrared (IR) pulse has been used as nonlinear interaction. Pulses as short as 3 fs have been measured in the whole tuning range. Kotsina and coworkers reported on temporal characterization of DUV pulses produced by RDW emission in HCFs using time-resolved photoelectron imaging (TRPEI) cross-correlation measurements based on non-resonant two-colour DUV-IR multiphoton ionization of 1,3-butadiene molecules [5]. DUV pulses were spectrally separated from the co-propagating residual IR and visible supercontinuum by a pair of broadband dichroic mirrors. From the energy integrated TRPEI data measured at DUV wavelengths centred at 250 and 280 nm, it was possible to retrieve a DUV pulse duration of ~ 6 fs. Zhang and coworkers [31] reported on the temporal characterization of UV pulses generated by RDW emission in gas-filled HCFs by Self-Diffraction Frequency-Resolved Optical Gating (SD-FROG) [32,33]: pulses as short as 9.4 fs at 430 nm were measured.

We report on the first direct temporal characterization of sub-3-fs pulses generated by RDW emission in HCFs, spectrally tunable in a broad DUV/UV spectral region. Temporal characterization has been achieved by using an all-in-vacuum SD-FROG.

2. Experimental setup

The experimental setup is shown in Fig. 1. Since the length of the HCF for RDW emission increases with the duration of the input pulse, a compression stage based on the HCF compression technique [13] was implemented to achieve a pulse duration of ~ 10 fs. 35-fs light pulses generated by a Ti:sapphire laser system (Coherent Astrella) at 1-kHz repetition rate are coupled into a 1-m-long HCF with a 320- μm core diameter, uniformly filled with neon (pressure $p = 2.2$ bar). The input and output pulse energies are 1.6 mJ and 1 mJ, respectively. The beam pointing at the input

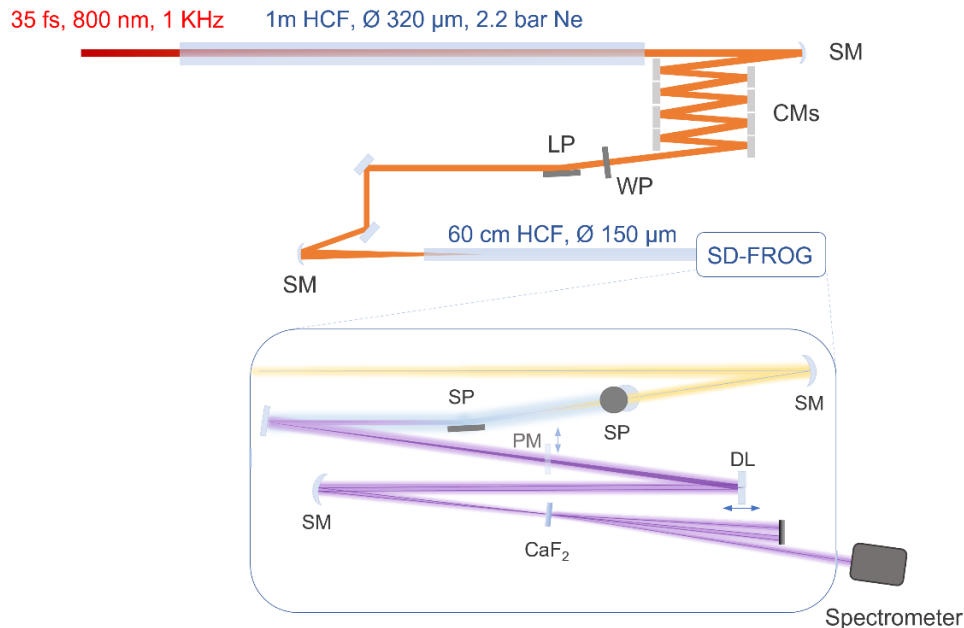


Fig. 1. Scheme of the experimental setup: 35-fs pulses centered at 800 nm are spectrally broadened in a 1-m-long HCF (320- μm core diameter) filled with neon. The pulses are then collimated by a spherical mirror (SM) and post compressed with a set of chirped mirrors (CMs). A half-wave plate (WP) and a linear polarizer (LP) serve as a variable attenuator. A second spherical mirror couples the beam into a 60-cm-long HCF (150- μm core diameter), mounted in a pressure gradient configuration. The DUV/UV pulses are spectrally filtered by two Brewster-angle silicon plates (SP) and divided into two replicas by two D-shaped mirrors, which act as a delay line (DL) since one of the two is mounted on a motorized translational stage. Both beams are focused onto a 50- μm -thick CaF_2 crystal yielding a self-diffraction signal, which is spatially isolated and measured by a spectrometer as a function of the temporal delay between the two replicas. PM is a pick-off mirror.

of the fiber is actively stabilized. 9.7 ± 0.2 -fs pulses are generated after dispersion compensation by chirped mirrors (transform-limited pulse duration is 6.5 fs); temporal characterization is carried out using second-harmonic FROG (SH-FROG). The compressed pulses are then coupled into a second 60-cm-long, stretched HCF [34], with a 150- μm core diameter, where RDW emission takes place. The pulse energy at the fiber input is adjusted by a variable attenuation stage made by a half-wave plate followed by a silicon plate at Brewster's angle ($\sim 75^\circ$) for IR pulses centered at 800 nm. This attenuation stage is crucial to achieve the pulse energy that optimizes the RDW process in the HCF. The use of an attenuation stage at the output of the first HCF is beneficial because it decouples the HCF used for RDW from the first compression stage, which is optimized to achieve an output pulse with a constant pulse duration of ~ 10 fs. Pulse energy up to 140 μJ was used for the experiments reported in this work. This corresponds to a maximum coupled pulse energy of 70 μJ at the input of the fiber (hereafter called input pulse energy), given the measured 50% coupling efficiency. A decreasing longitudinal gas pressure gradient along the waveguide is employed [35], in order to allow for an almost dispersion-free delivery of the RDW pulses into a vacuum system. This is particularly important in the DUV/UV spectral region due to the high dispersion of air ($\sim 80 \text{ fs}^2/\text{m}$ at 300 nm) and the fact that broadband dispersion compensation methods are unavailable in this spectral region. The experimental setup used to stretch the HCF is particularly suitable to achieve the required pressure gradient

configuration since the inlet and outlet ends of the HCF are sealed into two gas cells, which can be independently evacuated or filled with gas. The pressure at the output of the fiber is kept at $\sim 10^{-2}$ mbar with a roughing pump. The neon gas pressure at the fiber input and the energy of the driving IR pulses were adjusted to phase-match the RDW emission process.

The beam at the output of the second HCF is collimated in vacuum by a concave aluminum mirror and the RDW emission is spectrally filtered from the residual visible/IR portion of the driving pulses using two silicon plates at Brewster's angle, rejecting both the S and P polarization states of the driving radiation. The total reflectivity of the two Si plates decreases from $\sim 42\%$ at 210 nm to $\sim 4\%$ at 400 nm (it is $< 0.2\%$ in the wavelength range above 600 nm). This spectral separation setup is less efficient than dichroic mirrors, but the crucial advantage is its ultrabroad bandwidth. Indeed, efficient spectral selection can be achieved spanning from ~ 210 nm to ~ 400 nm. A pick-off mirror (PM in Fig. 1) is mounted on a translational stage just before the SD-FROG interferometer, to allow a direct path to the spectrometer and an independent measurement of the DUV/UV spectrum and energy.

The SD-FROG setup, shown in Fig. 1, starts with two aluminum split mirrors, which generate two pulse replicas. The relative temporal delay between the two pulses is adjusted by a piezoelectric stage on which one of the two split mirrors is mounted. The two pulse replicas are then focused onto a 50- μm -thick CaF_2 crystal. The interference intensity pattern is translated into a refractive index pattern by the Kerr effect in the crystal, which behaves as a transient grating. One of the two first-order diffracted beams is then spatially selected and its spectrum is measured as a function of the delay between the two pulse replicas, thus generating an SD-FROG spectrogram.

3. Fiber design criteria

The choice of the parameters of the stretched fiber in which the RDW emission process takes place, including fiber core size, fiber length, the type of gas used as nonlinear medium and its pressure range, has been performed by employing the model detailed in Ref. [22], which is based on the multi-mode unidirectional pulse propagation equation [36,37]. The model includes the waveguide [38] and gas [39] dispersion and the Kerr nonlinearity [40]. The effect of photoionization is included using the Perelomov-Popov-Terent'ev ionization rate [41–43], being a good approximation in the intensity regime of this work. We note that, even at the highest peak intensity used in the measurements ($\sim 2 \times 10^{14}$ W/cm²), the ionization fraction remains below 4×10^{-5} .

Since the setup for RDW emission will be employed for DUV/UV pump-EUV probe spectroscopy, a major criterion was the design of a compact setup. The length of the HCF is mainly determined by the distance over which soliton self-compression occurs, well approximated by the fission length, L_f , which is related to the gas used for RDW emission, to the fiber core radius, a , and to the characteristics of the input pulse by the following simple relation [22,44]

$$L_f \approx \frac{a^2 \tau}{3N|\delta(\lambda_0, \lambda_{zd})|} \propto \frac{a^2 \tau}{\sqrt{I_0}} \quad (1)$$

where: τ and I_0 are the duration and the peak intensity of the input pulse, respectively; N is the soliton order; $\delta(\lambda_0, \lambda_{zd})$ is a function that describes the dispersion of the gas inside the fiber; λ_0 is the central wavelength of the pulses at the input of the HCF and λ_{zd} is the zero dispersion wavelength (i.e., the wavelength where the group velocity dispersion vanishes). The combination of λ_0 and the pressure-dependent λ_{zd} determines the wavelength at which the RDW is emitted. The pulse peak power is limited by self-focusing [45] and the peak intensity is limited by the ionization of the gas, while the fiber core radius dictates the losses, since the field attenuation constant is inversely proportional to a^3 [38].

In the experimental setup we have used a HCF with a core diameter of 150 μm . A fiber length just slightly longer than the fission length is advantageous to avoid propagation of the generated DUV/UV pulses through the residual gas at the fiber exit, thus avoiding the introduction of temporal broadening due to positive dispersion, but still sufficient for the generation of the RDW pulses.

Figure 2 shows the simulated spectral evolution, as a function of the propagation distance inside the HCF, when neon is used as the nonlinear medium. In the simulations, a decreasing pressure gradient along the HCF has been assumed [46]:

$$p(z) = p_0 \sqrt{1 - \frac{z}{L}} \quad (2)$$

where p_0 is maximum pressure ($p_0 = 6.2$ bar for the simulation displayed in Fig. 2), at the fiber input, L is the fiber length and z is the position along the fiber. In the simulations the experimental temporal intensity profile of the input pump pulses has been used, and the pulse energy coupled into the HCF (25 μJ) has been determined by the transmission of the evacuated HCF. The simulation in Fig. 2 shows the generation of a supercontinuum upon propagation along the fiber, spanning from ~ 200 nm to ~ 1300 nm, corresponding, in the temporal domain, to soliton self-compression [22], and an efficient RDW emission around 300 nm, for propagation lengths greater than ~ 0.45 m. Furthermore, as shown later (see Figs. 4 and 5) the RDW emission is predicted to have durations in the sub-3-fs range.

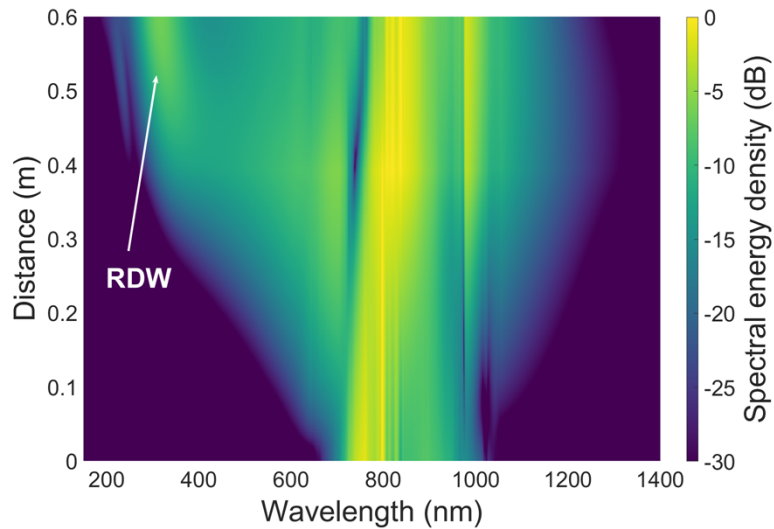


Fig. 2. Calculated spectral evolution, on a logarithmic color scale, of the pulse propagating along a HCF with a core diameter of 150 μm , filled with neon with decreasing pressure gradient. The gas pressure at the fiber input is $p_0 = 6.2$ bar. The experimental temporal intensity profile of the input pulses has been used (pulse duration: 9.7 fs, pulse energy: 25 μJ).

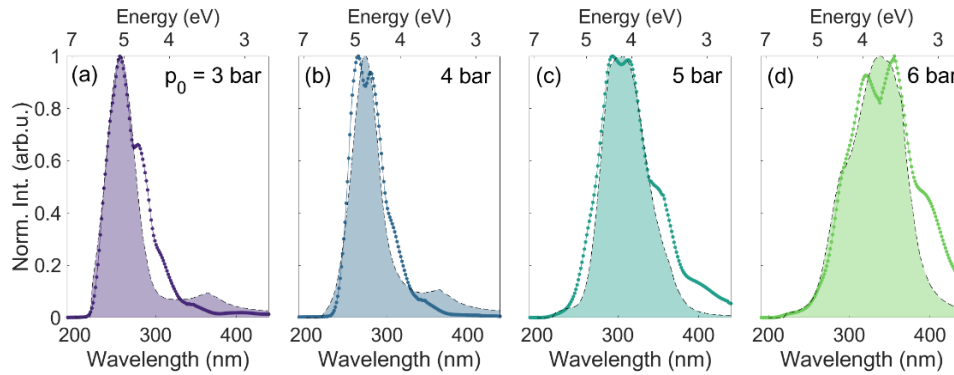


Fig. 3. Measured spectra of the RDW pulses generated in neon at different input pressure, p_0 , ranging from 3 to 6 bars (curves with dots). The dashed curves with shaded area are the spectra of the RDW pulses calculated using the numerical model described in Sect. 3, taking into account the reflectivity of the two Si plates and of the aluminum mirrors.

4. Experimental results

Figure 3 shows the measured pulse spectra at the output of the second HCF, filled with neon at four input pressures, p_0 , ranging from 3 bar to 6 bar. The central wavelength of the RDW pulses can be continuously tuned from ~ 250 nm to ~ 350 nm when the energy coupled to the second fiber is set to maximize the RDW emission bandwidth (the input pulse energy was varied between $25 \mu\text{J}$ and $70 \mu\text{J}$). The pressure at the fiber exit was kept constant at $\sim 10^{-2}$ mbar. The numerical simulations nicely reproduce the experimental results, as shown by the dashed curves in Fig. 3, upon assuming input pressures slightly higher than the experimental ones (see Table 1). The numerical simulations shown in Fig. 3 take into account the reflectivity of the two Si plates used to spectrally filter the RDW pulses and of the aluminum mirrors. Accounting for the transmission of the CaF_2 window and the losses due to reflection on the silicon plates and on the aluminum mirrors before the extraction, an estimation of the energy contained in the RDW pulses can be obtained, in the range between 2.4 and $4.1 \mu\text{J}$, depending on the experimental conditions (see Table 1).

Table 1. Characteristics of the RDW pulses generated at various neon pressures at the fiber input (p_0)^a

$p_{0,\text{exp}}$ (bar)	$p_{0,\text{sim}}$ (bar)	λ_{RDW} (nm)	E_{RDW} (μJ)	E_t (μJ)	τ_{RDW} (fs)
3	3.8	257	2.4	0.60	2.8 ± 0.1
4	4.4	265	2.7	0.75	3.0 ± 0.2
5	6.2	298	3.5	0.50	2.4 ± 0.1
6	6.8	352	4.1	0.35	2.4 ± 0.1

^apeak wavelength (λ_{RDW}), measured energy after Si plates (E_t), energy before Si plates estimated considering the total reflectivity of the two plates and aluminum mirrors used in the experimental setup (E_{RDW}), and FWHM-duration (τ_{RDW}). $p_{0,\text{exp}}$ and $p_{0,\text{sim}}$ are the experimental pressure and the pressure used in the simulations, respectively.

The temporal characterization of the RDW pulses has been performed using the SD-FROG technique. The two replicas of the RDW pulse produced by the split mirror used in the experimental setup (see Fig. 1) have been focused onto the CaF_2 crystal with a small crossing angle ($\sim 1.5^\circ$) to minimize the intrinsic phase-mismatch of the self-diffraction process. SD-FROG

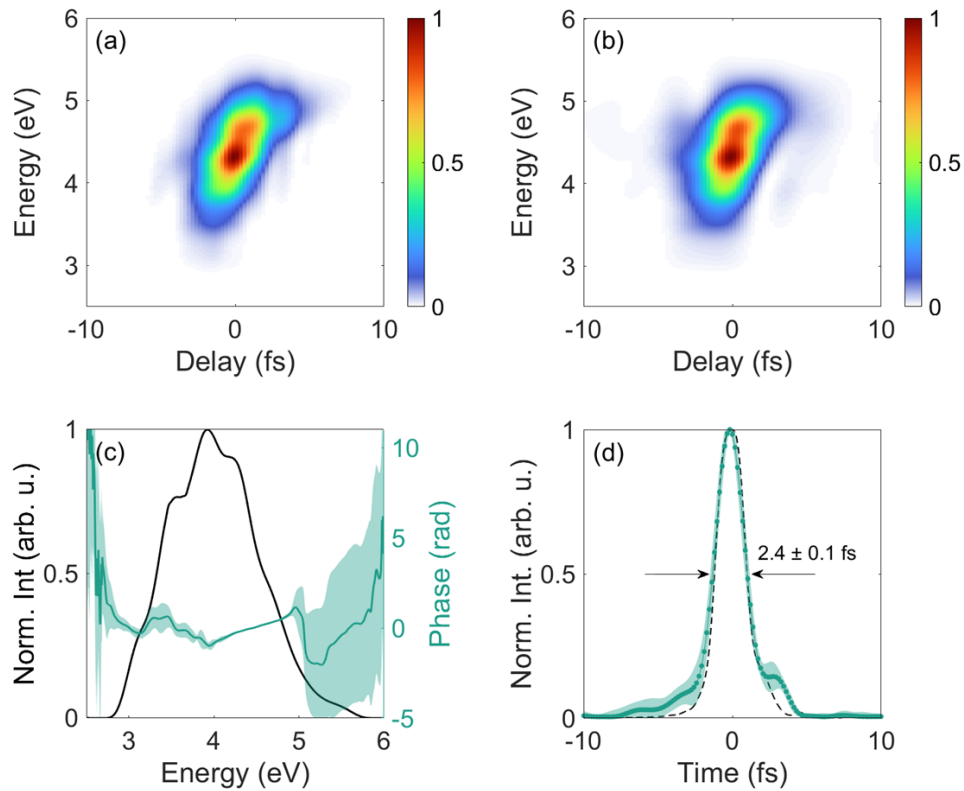


Fig. 4. Experimental (a) and retrieved (b) SD-FROG spectrograms of the RDW pulses generated in neon with $p_0 = 5$ bar input pressure. (c) Experimental spectrum (black line) and reconstructed spectral phase (green line) of the RDW pulse. (d) The dotted green curve represents the retrieved temporal intensity profile of the RDW pulse; the black dashed curve is the intensity profile calculated by using numerical simulations. Both in (c) and (d) the shaded green area represents the standard deviation obtained by comparing a set of 10 reconstructions. The initial conditions are random, each reconstruction is independent of the others due to the intrinsic randomness of the algorithm which starts from diverse initial conditions. Grid size: 4096 energy points \times 119 delay points; average error (over 10 reconstructions): 5.6×10^{-3} with a standard deviation of 0.4×10^{-3} .

spectrograms have been collected by spatially filtering one of the two first-order diffracted beams. Figure 4(a) shows the experimental SD-FROG spectrogram of the RDW pulses generated in neon with $p_0 = 5$ bar at the fiber input. An advantage of the SD-FROG traces is the lack of ambiguity in the presence of chirp and in its sign. The measured trace shows a small tilt, indicating the presence of a small positive chirp.

The measured SD-FROG traces were reconstructed through a phase-only retrieval approach, while the spectral intensity was independently measured and held constant during the reconstruction procedure. Among different evolutionary algorithms for phase retrieval, we implemented differential evolution (DE) [47,48]. Genetic algorithms were chosen for their ability to efficiently explore the large non-convex parameter space, while also being able to enforce physical constraints on the pulse generating the trace and incorporating problem-specific knowledge. In contrast, approaches such as the extended ptychographic iterative engine (ePIE) [49] or PCGPA do not enable to force both the spectrum and the phase to follow the physical constraint. In the implementation of ePIE the spectral amplitude of pulse and gate, $E^2(t)$ and $E^*(t)$, respectively

(in the case of SD-FROG), can be fixed to match the experimental spectrum, but the phases are totally independent, thus yielding two different results in terms of field. Forcing the correct relation between the two spectral phases would severely hamper the convergence of the algorithm. While it is still possible to obtain an estimate on the pulse duration by averaging the field extracted from the pulse and the field extracted from the gate, we chose to follow the genetic approach which permits to directly satisfy the physical constraints.

DE provides an efficient and robust tool, capable of handling noisy and incomplete data due to experimental limitations, such as a limited phase matching bandwidth of the nonlinear process. The implementation of DE utilized in this work is based on the best-of-random method detailed by Escoto *et al.* [47], adapted specifically for the retrieval of SD-FROG traces. To account for the limited phase-matching bandwidth of the nonlinear process and any spectral effects caused by detection, a spectral filter is generated at each iteration of the algorithm and applied to the retrieved traces before comparing them with the measured one. The retrieved trace after applying the filter is given by:

$$I_{rec}(\omega, \tau) = R(\omega)I_{sim}(\omega, \tau), \quad (3)$$

where $I_{sim}(\omega, \tau)$ is the simulated unfiltered trace obtained for a given guess of the spectral phase, and the spectral filter $R(\omega)$ is obtained as follows:

$$R(\omega) = \frac{\sum_j I_{meas}(\omega, \tau_j) I_{sim}(\omega, \tau_j)}{\sum_j I_{sim}(\omega, \tau_j)^2} \quad (4)$$

where $I_{meas}(\omega, \tau)$ is the measured trace. The filter is then employed in the calculation of the fitness parameter, which determines the guesses generated at each new iteration [47]. In order to prevent numerical artifacts in the retrieval that can result in non-physical solutions such as sudden 2π jumps or unwanted oscillations, it was necessary to impose that the spectral phase of the pulses be well behaved. The phase was regularized using interpolation over a randomly selected portion of the frequency points over which it was defined, utilizing the modified Akima formula [50]. This method was chosen over spline-based interpolation due to its ability to produce fewer non-physical oscillations in the retrieved phase. Due to the random initial conditions and the intrinsic randomness of the algorithm, each reconstruction is independent of the others and may converge towards a slightly different solution. To estimate the retrieved duration and the error of the retrieval, 10 reconstructions were performed for each experimental trace. The temporal profile of the retrieved pulse is given by the average of the temporal profiles obtained from each reconstruction, while their standard deviation provides an estimate of the error. Similarly, the retrieved spectral phase is taken as the average of the retrieved phases, after removing any constant offset and linear component. The averaging is performed over the real and imaginary parts of the complex spectrum, yielding an average complex spectrum, the phase of which gives the average spectral phase of the pulses.

The retrieved SD-FROG spectrogram is displayed in Fig. 4(b), which is in excellent agreement with the measured trace of Fig. 4(a). Figures 4(c) and 4(d) show the retrieved spectral phase and temporal intensity profile, respectively, of the RDW pulse. A duration of 2.4 ± 0.1 fs (FWHM) has been obtained (to be compared to a transform-limited duration of 1.9 fs). The dashed curve in Fig. 4(d) is the temporal intensity profile of the RDW pulse calculated using the numerical simulations described in Sect. 3, in reasonably good agreement with the experimental result. The uncertainties on the retrieved temporal profile and spectral phase are taken as the standard deviation of the relative quantities for the 10 retrievals (shown as shaded areas in Figs. 4(c) and 4(d)). It is worth noting that the large standard deviation of the reconstructed spectral phase (Fig. 4(c)) outside the central region of the spectrum, caused by the limited phase-matching bandwidth of the nonlinear process, does not lead to significant modifications of the reconstructed intensity profiles of the RDW pulse (Fig. 4(d)).

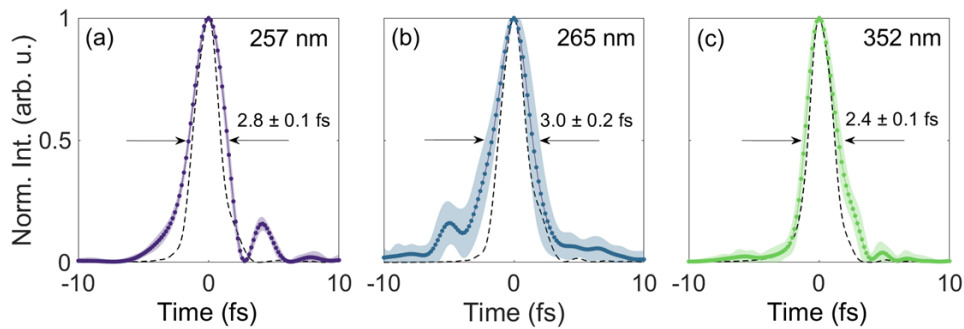


Fig. 5. Temporal intensity profile of the RDW pulses for three values of the neon pressure ((a) $p_0 = 3$ bar, (b) $p_0 = 4$ bar and (c) $p_0 = 6$ bar) retrieved from the SD-FROG spectrograms (lines with dots); the shaded area represents the standard deviation obtained by comparing a set of 10 reconstructions. The initial conditions are random, each reconstruction is independent of the others due to the intrinsic randomness of the algorithm. The black dashed curves are the intensity profiles calculated by using the numerical model described in Sect. 3.

Using the same procedure, the RDW pulse duration was measured while varying the neon pressure from 3 bar to 6 bar. Figure 5 shows the temporal intensity profiles retrieved from the SD-FROG spectrograms (dots, the shaded areas correspond to the standard deviation) and those calculated by using the numerical simulations described in Sect. 3. Pulse durations in the range between 2.4 fs and 3 fs have been obtained in the whole tuning spectral region. Table 1 reports the peak wavelength, the energy and the FWHM duration of the RDW pulses generated by varying the neon pressure.

5. Conclusions

We presented the generation and complete temporal characterization of tunable DUV/UV pulses, generated by resonant dispersive wave emission in hollow-capillary fibers, filled with gas. Sub-3-fs pulses with energy in the μJ -range were generated, with central wavelength continuously tunable from 250 nm to 350 nm. Temporal characterization was achieved by implementing an all-in-vacuum SD-FROG apparatus with an optimized reconstruction procedure. By using a decreasing pressure gradient configuration, the pulses are delivered in vacuum, thus making it possible to directly couple the experimental setup with an EUV attosecond beamline. We believe that this experimental approach has great potential in the field of ultrafast spectroscopy, in particular for pump-probe measurements with extreme temporal resolution, when combined with attosecond EUV and soft x-ray pulses.

Funding. European Research Council (ERC-SyG 951224 TOMATTO, ERC-StG 679649 HISOL, ERC-CoG 101001534 XSOL, ERC-StG 848411 AuDACE, ERC-MSCA-IF 10102311 HETRUSQ); Ministero dell’Istruzione, dell’Università e della Ricerca (20173B72NB); Fondazione Cariplo (2020-4380); Royal Academy of Engineering (RF/202122/21/133).

Disclosures. The authors declare no conflicts of interest.

Data availability. Data underlying the results presented in this paper are not publicly available at this time but may be obtained from the authors upon reasonable request.

References

1. M. Chergui, “Ultrafast molecular photophysics in the deep-ultraviolet,” *J. Chem. Phys.* **150**(7), 070901 (2019).
2. R. Borrego-Varillas, D. C. Teles-Ferreira, A. Nenov, I. Conti, L. Ganzer, C. Manzoni, M. Garavelli, A. M. de Paula, and G. Cerullo, “Observation of the Sub-100 Femtosecond Population of a Dark State in a Thiobase Mediating Intersystem Crossing,” *J. Am. Chem. Soc.* **140**(47), 16087–16093 (2018).

3. R. Borrego-Varillas, A. Nenov, P. Kabaciński, I. Conti, L. Ganzer, A. Oriana, V. K. Jaiswal, I. Delfino, O. Weingart, C. Manzoni, I. Rivalta, M. Garavelli, and G. Cerullo, "Tracking excited state decay mechanisms of pyrimidine nucleosides in real time," *Nat. Commun.* **12**(1), 7285 (2021).
4. V. K. Jaiswal, P. Kabaciński, E. Barbara, N. de Faria, M. Gentile, A. M. de Paula, R. Borrego-Varillas, A. Nenov, I. Conti, G. Cerullo, and M. Garavelli, "Environment-Driven Coherent Population Transfer Governs the Ultrafast Photophysics of Tryptophan," *J. Am. Chem. Soc.* **144**(28), 12884–12892 (2022).
5. N. Kotsina, C. Brahms, S. L. Jackson, J. C. Travers, and D. Townsend, "Spectroscopic application of few-femtosecond deep-ultraviolet laser pulses from resonant dispersive wave emission in a hollow capillary fibre," *Chem. Sci.* **13**(33), 9586–9594 (2022).
6. R. Borrego-Varillas, L. Ganzer, G. Cerullo, and C. Manzoni, "Ultraviolet Transient Absorption Spectrometer with Sub-20-fs Time Resolution," *Appl. Sci.* **8**(6), 989–1006 (2018).
7. L. Cederbaum and J. Zobeley, "Ultrafast charge migration by electron correlation," *Chem. Phys. Lett.* **307**(3-4), 205–210 (1999).
8. F. Remacle and R. D. Levine, "An electronic time scale in chemistry," *Proc. Natl. Acad. Sci. U. S. A.* **103**(18), 6793–6798 (2006).
9. F. Calegari, D. Ayuso, A. Trabattoni, L. Belshaw, S. De Camillis, S. Anumula, F. Frassetto, L. Poletto, A. Palacios, P. Decleva, J. Greenwood, F. Martín, and M. Nisoli, "Ultrafast Electron Dynamics in Phenylalanine Initiated by Attosecond Pulses," *Science* **346**(6207), 336–339 (2014).
10. R. Borrego-Varillas, M. Lucchini, and M. Nisoli, "Attosecond spectroscopy for the investigation of ultrafast dynamics in atomic, molecular and solid-state physics," *Rep. Prog. Phys.* **85**(6), 066401 (2022).
11. M. Nisoli, P. Decleva, F. Calegari, A. Palacios, and F. Martín, "Attosecond electron dynamics in molecules," *Chem. Rev.* **117**(16), 10760–10825 (2017).
12. I. C. D. Merritt, D. Jacquemin, and M. Vacher, "Attochemistry: Is Controlling Electrons the Future of Photochemistry?" *J. Phys. Chem. Lett.* **12**(34), 8404–8415 (2021).
13. M. Nisoli, S. D. Silvestri, and O. Svelto, "Generation of high energy 10 fs pulses by a new pulse compression technique," *Appl. Phys. Lett.* **68**(20), 2793–2795 (1996).
14. D. Brida, C. Manzoni, G. Cirmi, M. Marangoni, S. Bonora, P. Villorosi, S. De Silvestri, and G. Cerullo, "Few-optical-cycle pulses tunable from the visible to the mid-infrared by optical parametric amplifiers," *J. Opt.* **12**(1), 013001 (2010).
15. V. Wanie, L. Colaizzi, A. Cartella, A. Trabattoni, and F. Calegari, "Advances of ultraviolet light sources: towards femtosecond pulses in the few-cycle regime," in *Emerging Laser Technologies for High-Power and Ultrafast Science*, F. Légaré, ed. (IOP Publishing Ltd, 2021), Chap. 5.
16. P. Baum, S. Lochbrunner, and E. Riedle, "Tunable sub-10-fs ultraviolet pulses generated by achromatic frequency doubling," *Opt. Lett.* **29**(14), 1686–1688 (2004).
17. P. Baum and E. Riedle, "Design and calibration of zero-additional-phase SPIDER," *J. Opt. Soc. Am. B* **22**(9), 1875–1883 (2005).
18. C. G. Durfee III, S. Backus, H. C. Kapteyn, and M. M. Murnane, "Intense 8-fs pulse generation in the deep ultraviolet," *Opt. Lett.* **24**(10), 697–699 (1999).
19. Y. Kida, J. Liu, T. Teramoto, and T. Kobayashi, "Sub-10 fs deep-ultraviolet pulses generated by chirped-pulse four-wave mixing," *Opt. Lett.* **35**(11), 1807–1809 (2010).
20. F. Reiter, U. Graf, M. Schultze, W. Schweinberger, H. Schröder, N. Karpowicz, A. M. Azeze, R. Kienberger, F. Krausz, and E. Goulielmakis, "Generation of sub-3 fs pulses in the deep ultraviolet," *Opt. Lett.* **35**(13), 2248–2250 (2010).
21. M. Galli, V. Wanie, D. P. Lopes, E. P. Mansson, A. Trabattoni, L. Colaizzi, K. Saraswathula, A. Cartella, F. Frassetto, L. Poletto, F. Légaré, S. Stagira, M. Nisoli, R. M. Vazquez, R. Osellame, and F. Calegari, "Generation of deep ultraviolet sub-2-fs pulses," *Opt. Lett.* **44**(6), 1308–1311 (2019).
22. J. C. Travers, T. F. Grigorova, C. Brahms, and F. Belli, "High-energy pulse self-compression and ultraviolet generation through soliton dynamics in hollow capillary fibres," *Nat. Photonics* **13**(8), 547–554 (2019).
23. F. Köttig, F. Tani, C. M. Biersach, J. C. Travers, and P. S. J. Russell, "Generation of microjoule pulses in the deep ultraviolet at megahertz repetition rates," *Optica* **4**(10), 1272–1276 (2017).
24. P. K. A. Wai, C. R. Menyuk, Y. C. Lee, and H. H. Chen, "Nonlinear pulse propagation in the neighborhood of the zero-dispersion wavelength of monomode optical fibers," *Opt. Lett.* **11**(7), 464–466 (1986).
25. V. I. Karpman, "Radiation by solitons due to higher-order dispersion," *Phys. Rev. E* **47**(3), 2073–2082 (1993).
26. N. Akhmediev and M. Karlsson, "Cherenkov radiation emitted by solitons in optical fibers," *Phys. Rev. A* **51**(3), 2602–2607 (1995).
27. J. N. Elgin, T. Brabec, and S. M. J. Kelly, "A perturbative theory of soliton propagation in the presence of third order dispersion," *Opt. Commun.* **114**(3-4), 321–328 (1995).
28. D. V. Skryabin and A. V. Gorbach, "Looking at a soliton through the prism of optical supercontinuum," *Rev. Mod. Phys.* **82**(2), 1287–1299 (2010).
29. A. Ermolov, H. Valtna-Lukner, J. Travers, and P. S. J. Russell, "Characterization of few-fs deep-UV dispersive waves by ultra-broadband transient-grating XFROG," *Opt. Lett.* **41**(23), 5535–5538 (2016).

30. C. Brahms, D. R. Austin, F. Tani, A. S. Johnson, D. Garratt, J. C. Travers, J. W. G. Tisch, P. S. J. Russell, and J. P. Marangos, "Direct characterization of tuneable few-femtosecond dispersive-wave pulses in the deep UV," *Opt. Lett.* **44**(4), 731–734 (2019).
31. C. Zhang, T. Chen, J. Pan, Z. Huang, D. Liu, D. Wang, F. Yu, D. Wu, Y. Zheng, R. Yin, X. Jiang, M. Pang, Y. Leng, and R. Li, "Measurements of microjoule-level, few-femtosecond ultraviolet dispersive-wave pulses generated in gas-filled hollow capillary fibers," *Opt. Lett.* **47**(18), 4830–4833 (2022).
32. D. J. Kane and R. Trebino, "Characterization of arbitrary femtosecond pulses using frequency-resolved optical gating," *IEEE J. Quantum Electron.* **29**(2), 571–579 (1993).
33. S. Backus, J. Peatross, Z. Zeek, A. Rundquist, G. Taft, M. M. Murnane, and H. C. Kapteyn, "16-fs, 1- μ J ultraviolet pulses generated by third-harmonic conversion in air," *Opt. Lett.* **21**(9), 665–667 (1996).
34. T. Nagy, M. Forster, and P. Simon, "Flexible hollow fiber for pulse compressors," *Appl. Opt.* **47**(18), 3264–3268 (2008).
35. C. Brahms, F. Belli, and J. C. Travers, "Resonant dispersive wave emission in hollow capillary fibers filled with pressure gradients," *Opt. Lett.* **45**(16), 4456–4459 (2020).
36. A. Couairon, E. Brambilla, T. Corti, D. Majus, O. D. J. Ramírez-Góngora, and M. Kolesik, "Practitioner's guide to laser pulse propagation models and simulation: Numerical implementation and practical usage of modern pulse propagation models," *Eur. Phys. J. Spec. Top.* **199**(1), 5–76 (2011).
37. F. Tani, J. C. Travers, and P. S. J. Russell, "Multimode ultrafast nonlinear optics in optical waveguides: numerical modeling and experiments in kagomé photonic-crystal fiber," *J. Opt. Soc. Am. B* **31**(2), 311–320 (2014).
38. E. A. J. Marcatili and R. A. Schmeltzer, "Hollow Metallic and Dielectric Waveguides for Long Distance Optical Transmission and Lasers," *Bell Syst. Tech. J.* **43**(4), 1783–1809 (1964).
39. A. Börzsönyi, Z. Heiner, M. P. Kalashnikov, A. P. Kovács, and K. Osvay, "Dispersion measurement of inert gases and gas mixtures at 800 nm," *Appl. Opt.* **47**(27), 4856–4863 (2008).
40. D. P. Shelton and J. E. Rice, "Measurements and calculations of the hyperpolarizabilities of atoms and small molecules in the gas phase," *Chem. Rev.* **94**(1), 3–29 (1994).
41. A. M. Perelomov, V. S. Popov, and M. V. Terent'ev, "Ionization of atoms in an alternating electric field," *Sov. Phys. JETP* **23**(5), 1393–1409 (1966).
42. M. Geissler, G. Tempea, A. Scrinzi, M. Schnürer, F. Krausz, and T. Brabec, "Light Propagation in Field-Ionizing Media: Extreme Nonlinear Optics," *Phys. Rev. Lett.* **83**(15), 2930–2933 (1999).
43. C. Brahms and J. C. Travers, *Luna.jl*, *Zenodo* (2022).
44. C. Brahms, T. Grigorova, F. Belli, and J. C. Travers, "High-energy ultraviolet dispersive-wave emission in compact hollow capillary systems," *Opt. Lett.* **44**(12), 2990–2993 (2019).
45. G. Fibich and A. L. Gaeta, "Critical power for self-focusing in bulk media and in hollow waveguides," *Opt. Lett.* **25**(5), 335–337 (2000).
46. A. Suda, M. Hatayama, K. Nagasaka, and K. Midorikawa, "Generation of sub-10-fs, 5-mJ-optical pulses using a hollow fiber with a pressure gradient," *Appl. Phys. Lett.* **86**(11), 111116 (2005).
47. E. Escoto, A. Tajalli, T. Nagy, and G. Steinmeyer, "Advanced phase retrieval for dispersion scan: a comparative study," *J. Opt. Soc. Am. B* **35**(1), 8–19 (2018).
48. S. Das and P. N. Sugathan, "Differential evolution: A survey of the state-of-the-art," *IEEE Trans. Evol. Computat.* **15**(1), 4–31 (2011).
49. M. Lucchini, M. Brüggemann, A. Ludwig, L. Gallmann, U. Keller, and T. Feurer, "Ptychographic reconstruction of attosecond pulses," *Opt. Express* **23**(23), 29502–29513 (2015).
50. H. Akima, "A New Method of Interpolation and Smooth Curve Fitting Based on Local Procedures," *J. Assoc. Comput. Mach.* **17**(4), 589–602 (1970).